

Elucidating Cycling Rate-Dependent Electrochemical Strains in Sodium Iron Phosphate Cathodes for Na-ion Batteries

Bertan Özdogru,^{‡a} Hannah Dykes,^{‡a} Darrell Gregory,^a Damien Saurel,^b Vijayakumar Murugesan,^c Montse Casas-Cabanas^b and Ö. Özgür Çapraz^{*a}

^a: The School of Chemical Engineering, Oklahoma State University, Stillwater, OK 74078.

^b: CIC EnergiGUNE, Parque Tecnológico de Álava, 01510, Vitoria-Gasteiz, Álava, Spain

^c: Joint Center for Energy Storage Research (JCESR), Pacific Northwest National Laboratory, 902 Battelle Blvd, Richland, WA 99354

*: Corresponding Author

‡: These authors contributed equally to this work.

ABSTRACT

Battery electrodes materials undergo significant mechanical instabilities which affects their longevity and exert rate-limitations during the cycling process. In this study, we investigate the rate-dependent mechanical response of sodium iron phosphate (NaFePO₄, NFP) cathodes during Na intercalation via galvanostatic cycling at different rates by employing digital image correlation, electrochemical methods, and mathematical model. The mechanical behaviour of the electrode shows strong dependance on the applied scan rate. At slower rates, electrode shows asymmetrical strain generation between anodic and cathodic cycles, which is attributed to the formation of cathode-electrolyte interface layers. The electrode undergoes smaller strain generation when cycled at slower rates when the same amount of Na ions is removed or inserted into the electrode. A mathematical model was developed to predict strain evolution in the composite electrode as well as the concentration profile of the Na ions in the electrode particles. Rate-dependent and time-dependent factors on the strain generation in the electrode are attributed to the capacity-dependent intercalation strains, rate-dependent mismatch strains, and time-dependent irreversible strains. The combination of in situ strain measurements with the analytical model provided new insight into the electrochemically induced mechanical deformations in Na-ion cathode electrodes.

KEYWORDS: Na-ion battery, rate dependent strain, digital image correlation, Sodium iron phosphate

1. INTRODUCTION

Recent concerns revolving around the relative scarcity and cost of lithium have resulted in increasing interest in rechargeable Na-ion batteries [1,2]. Sodium is a far more abundant material than lithium and is more evenly distributed throughout the earth crust [3]. However, Na-ion batteries suffer from low capacity retention due to chemo-mechanical degradations in the electrodes such as the decomposition of organic electrolytes on the surface of the electrode, continuous volumetric changes in the electrode constrained by current collectors, and mechanical damages in the electrodes [4,5]. Organic electrolytes decompose on the electrode surface during ion intercalation, causing the formation of a resistive surface layer on the electrode. Phase transitions commonly occur as Na ions intercalate into or out of the host lattice which creates volume mismatches. The associated misfit strains can produce plastic deformation or amorphization in the electrode material and have negative impacts on reversible ion insertion and extraction processes [6,7]. These chemo-mechanical degradations can be further exacerbated by the larger ionic radius of Na cations (1.02 Å) and their reactivity towards electrolyte species [8]. Also, it is expected that a cathode electrode would be prone to mechanical deformations during Na ion intercalation at faster rates due to kinetic limitation associated with slower Na ion diffusion. Although these chemo-mechanical deformations have been intensively reported for Li-ion battery electrodes, the physical response of the electrode upon Na intercalation is expected to be different than ones during Li intercalation. Therefore, further studies are required to understand the impact of the Na ions on the mechanical stability of electrodes.

Structural and interfacial instabilities in Li-ion battery electrodes have been studied by using an analytical mathematical model and various advanced characterization techniques such as electron microscopy [9–16], atomic force microscopy [17–21], in-situ XRD, and X-ray tomography [22–24], dilatometry [25,26], digital image correlation [27–29], and *in-situ* curvature measurements [30,31]. Transport-mechanics couplings in the electrified interfaces and bulk behavior of battery electrodes have been investigated by developing a continuum-based model for Li-ion batteries. These models enable the prediction of intercalation behavior of Li-ions under various factors such as surface tension, scan-rate, and morphology of the electrode [32–38]. The physical response of the Li-ion battery electrodes due to chemo-mechanical deformations has been characterized experimentally by monitoring stress and strain evolutions in the electrode via digital image correlation and curvature measurements. These in situ mechanical measurements shed light

on complex reaction processes controlling the stability of electrode structure as well as its surface with electrolyte [27,28,30,31,39]. However, chemo-mechanical instabilities associated with interfacial and structural deformations in the cathode electrodes during Na ion intercalation are not well known.

In this study, we chose sodium iron phosphate cathode to study rate-dependent and time-dependent deformations by utilizing in situ electrochemical strains, electrochemical techniques, and a mathematical model. Olivine-type sodium iron phosphate (NaFePO_4 , NFP) is structurally analogous to the Lithium iron phosphate (LiFePO_4 , LFP) electrode, which is an inexpensive and environmentally benign cathode material widely used in commercial Li-ion batteries. Due to the performance of the iron phosphate framework in Li-ion batteries, NFP has attracted much attention as a cathode electrode for Na-ion batteries. NFP has a theoretical capacity of 154 mAh g^{-1} . Michaelis group investigated the intercalation kinetics and electrochemical performance of NFP by using the electrochemical displacement technique [40,41]. Casas-Cabanas group monitored reaction mechanisms and associated structural deformations in the NFP electrodes via in situ x-ray diffractions [42–46]. Previously, we developed a methodology to tackle in situ electrochemical strain evolution in sodium iron phosphate electrodes using digital image correlation [27].

The goal of the study is to explore the rate and time effect on the mechanical behavior of the composite sodium iron phosphate cathode. To achieve it, we experimentally monitor in situ strain evolution in the electrode at different rates. In situ strains are monitored using the optical, full-field digital image correlation (DIC) technique. As expected, sodium intercalation causes volumetric expansions in the composite electrode and the volume of the electrode shrinks during the removal of Na ions. Although a large amount of the irreversible strain was detected during the first cycle, strains become reversible in the subsequent cycles. Noticeably larger expansions are observed in the composite electrode when cycled at faster scan rates. Strain evolution in the composite electrode is predicted based on the elastic properties of the composite electrode and atomic-scale changes in the crystal structures. Concentration gradients and mismatch strains inside the particles are also predicted based on the transport model. The experimental and modeling studies demonstrate the mechanical penalty in the NaFePO_4 composite electrode at faster rates.

2. MATERIALS AND METHODS

2.1. Material Preparation: Composite electrodes and electrolytes were prepared by following the procedure described previously[27]. Briefly, sodium carboxymethyl cellulose (binder, CMC, average MW ~700,000, Aldrich) and ultra-pure water mixed with 1:40 mass ratio and homogenized. Then, lithium iron phosphate (active material, LFP, Hanwha Chemical) and Super P (conductive additive, carbon black, >99%, metal basis, Alfa Aesar) were added to the above solution. The average particle size of LFP used in the study was 250 nm, determined by SEM. Final LFP: SuperP: CMC: Water mass ratio was 8:1:1:40. This slurry was mixed for 30 minutes with Thinky centrifugal mixer at 2000 rpm until completely homogenizes. To prepare the free-standing electrodes, the slurry was cast on copper foil (9 μm thick, >99.99%, MTT) and a doctor blade was used to control the slurry thickness. The casted slurry was air-dried at ambient condition for 16 h. Dried electrodes are carefully removed from the surface to create the free-standing electrodes used in the strain measurements. For coin cell and GITT measurements, the same slurry was prepared, and it was cast on aluminum foil (15 μm thick, MTT) with a doctor blade and air-dried for 16 h.

The electrolyte solution was prepared inside a glove box under an argon atmosphere (MB-Unilab Pro SP, MBRAUN). Oxygen and water contents were kept below 1 ppm all the time. Ethylene carbonate (EC, anhydrous, 99%, Acros Organics) and dimethyl carbonate (DMC, anhydrous, >99%, Aldrich) were mixed in a 1:1 volume ratio. 1 M sodium perchlorate (NaClO_4 , ACS grade, >98%, Aldrich) was added to the above EC/DMC solution.

Sodium cubes immersed in mineral oil (Na, 99.9%, metal basis, Sigma Aldrich) were cleaned with hexane inside the glove box. Cleaned Na cubes were stored in 1:1 (v:v) EC:DMC solution for future use. Before studies, Na cubes were removed from the solvent solution and dried with filter paper. A stainless-steel scalpel is used to clean the oxidized surface. The cleaned piece was then placed inside a polyethylene bag and rolled into the shape of a foil using a rolling pin. Flattened Na foil was then placed into the battery cell as a counter electrode.

2.2. Electrochemical Cycling: Electrochemical displacement technique was used to form iron phosphate (FP) composite electrode using pristine LFP composite electrode [27,40,41]. Electrochemical delithiation of the pristine LFP electrode was done by applying a positive current at $C/10$ rate to 4.0 V vs Na counter electrode. FP composite electrodes were cycled against Na counter electrode in 1 M NaClO_4 in 1:1 (v:v) EC:DMC electrolyte between 2.0-4.0 V. We provided further details of the electrochemical displacement technique in the Supplementary information by conducting X-ray diffraction analysis and in situ strain measurements. The electrodes were cycled at $C/25$, $C/10$, $C/4$ and $1C$ rates. GITT measurements were carried

out using a custom Swagelok coin cell system. Pristine LFP electrode cast on aluminum foil assembled into the custom cell with or Na counter electrode and electrolyte. A Celgrad 2044 polymer separator was used to separate both electrodes. Before GITT measurements, cells were cycled at a C/10 rate for 5 cycles. GITT measurements carried out with a series of current pulses at C/25 for 1 h, followed by a 10 h relaxation period.

2.3. Strain Measurements: A detailed description of the custom battery cell was provided in our previous publications [47]. Polychlorotrifluoroethylene (PCTFE, Plastics International) was used to make the main body of the custom battery cell and the electrode holders. Optical access was achieved by a quartz window (99.995 % SiO₂, 1/16 in thick, 2 in diameter, McMaster-Carr). This window was placed on the top of the custom cell and Viton O-rings (Grainger) used to seal the cell. Strain analysis was conducted by taking images of the freestanding electrode throughout the electrochemical cycling periods. Grasshopper3 5.0 MP camera (Sony IMX250, resolution, 2448 (w)*2048(h) pixel) with 12.0X adjustable zoom lens (NAVITAR) for an effective resolution of 0.873 $\mu\text{m}/\text{pixel}$ was used for image capture. Illumination of the freestanding electrode was achieved with a single constant high-intensity LED light source (Amazon). Depending on the cycling rate, images were captured every 10 min, 2 min, and 0.25 min for galvanostatic cycling at C/25, C/10, and C rates, respectively. A lab-made LabVIEW program was used to capture the images. The natural speckle pattern of the LFP composite electrode was used to calculate the strain generation on the electrode using Digital Image Correlation (DIC). Full-field strain measurements were performed on an area of interest of 750 $\mu\text{m}(\text{w}) \times 500 \mu\text{m}(\text{h})$ using Vic2D software with a subset size of 111 x 111 pixels and a step size of 15. Strains were synchronized with the electrochemical response of the electrodes (current and voltage) using a lab-made MATLAB program.

3. Results and Discussion

3.1. Representative Electrode Response during Na⁺ ion Intercalation: Figure 1A shows the representative electrochemical behavior of a sodium iron phosphate (NFP) composite electrode cycled galvanostatically at a C/25 rate against a sodium counter electrode for four cycles. Iron phosphate composite electrodes were formed by electrochemical displacement of Li ions from pristine lithium iron phosphate composite electrode using the methodology described in our previous publication [27]. Voltage and strain evolution during electrochemical delithiation of pristine LFP and resulting crystalline structure change can be seen in Supp. Figure 1. The sodiation of the iron phosphate in the first discharge resulted in 144mAh g⁻¹ discharge capacity,

which is close to the theoretical capacity of sodium iron phosphate (154 mAh g^{-1}) [40,41]. The electrode showed a very flat potential plateau around 2.85 V during the sodiation of iron phosphate in the first discharge. The discharge capacity decreased to 138 and 130 mAh g^{-1} in the second and fourth discharge cycles. Charge capacities during the first, second, and fourth cycles were calculated to be 174 , 164 , and 158 mAh g^{-1} , respectively. Two distinct potential plateaus at around 2.88 and 3.10 V were recorded during the first charge (desodiation). The evolution of the potential plateaus in the subsequent cycles was similar to the first cycle. A similar potential response during Na ion intercalation of NaFePO_4 electrodes via galvanostatic cycling was reported in the literature [40,41].

The corresponding strain evolution in the sodium iron phosphate composite electrode cycled at $C/25$ rate is shown in Figure 1B. Electrochemical strains demonstrated a linear relationship with galvanostatic charge/discharge time at all cycle numbers. As expected, electrochemical strains increased and decreased during the discharge and charge cycles, respectively. Strains

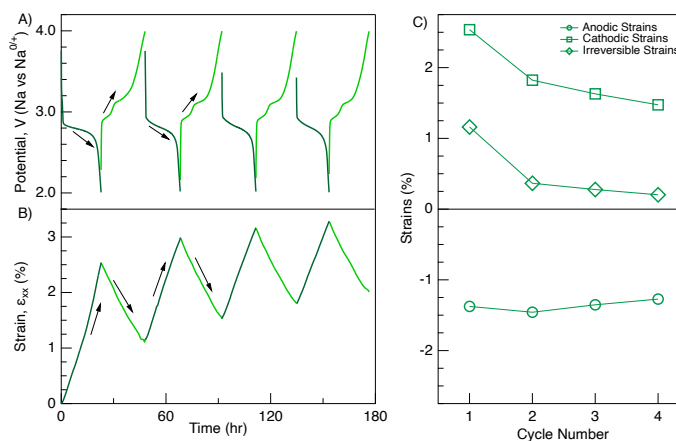


Figure 1: A) Voltage and B) strain evolution in iron phosphate composite electrode during sodium intercalation during cycling at $C/25$ in 1 M NaClO_4 in EC/DMC electrolyte. C) Corresponding anodic, cathodic, and irreversible strain generations.

were categorized as “anodic”, “cathodic” and “irreversible strain” to evaluate their progression with cycle numbers [48]. Anodic and cathodic strain values were shifted to start from zero at the beginning of each charge/discharge cycle to calculate strain generation in each cycle. The strain value at each cycle was labeled as “irreversible strain” and it was calculated by subtracting the cathodic strain from anodic strains for each cycle. During the first discharge cycle, the insertion of Na ions into iron phosphate resulted in 2.43% volume expansion in the NFP composite electrode. Cathodic strain progressively decreased from 2.43% at 1st discharge to 1.48% at 2nd discharge. The cathodic strains became 1.34 and 1.26% at the end of the 3rd and 4th discharge cycle, respectively. The removal of Na ions during the first charge cycle caused a reduction in electrode volume, generating about $-1.34 \pm 0.1\%$ anodic strain in the first charge cycle. However, there is an asymmetrical strain evolution in magnitude between charge and discharge cycles, causing mechanical irreversibility between anodic and cathodic cycles. At the end of the first cycle, the

electrode did not return to its original size, which results in 1.16% irreversible strains. In the subsequent cycles, the generation of the irreversible strains at each cycle reduced slowly from 0.36% at the end of the second cycle to 0.20 % at the end of the fourth cycle.

Strain and capacity derivatives with respect to potential are calculated to investigate the reversible changes in the electrode during Na ion intercalation. The angstrom-scale changes in the electrode structure during metal ion intercalation induce macroscale volumetric expansions in the composite electrode. Previous studies demonstrated a good correlation

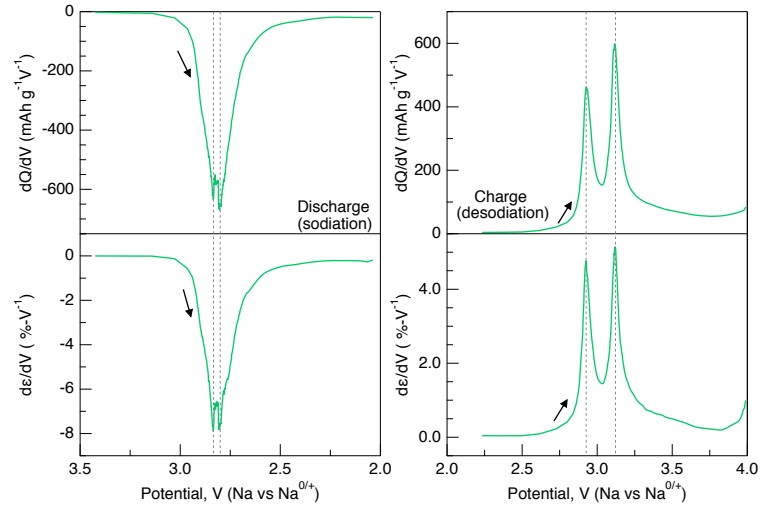


Figure 2: Capacity derivatives and strain derivatives in NaFePO₄ composite electrode cycled at C/25 during sodiation (left size) and desodiation (right side) in 1 M NaClO₄ in EC/DMC electrolyte during 4th cycle.

between phase transformations and the evolution of potential-dependent strain rates in the composite graphite, lithium iron phosphate, and lithium manganese oxide electrodes for Li-ion batteries [27,49–52]. The location of strain derivative peaks in these studies matches very well with the current peaks in cyclic voltammetry or the capacity derivative peaks in galvanostatic cycling. Similar to the previous studies, the strain derivatives, $d\varepsilon/dE$ and capacity derivatives, dQ/dE were calculated with respect to potential. Figure 2 shows strain and capacity derivatives during fourth charge and discharge cycles at C/25 rate. Two characteristic peaks in capacity derivatives are observed during fourth charge cycle at 2.92 and 3.11 V in Figure 2. A well-defined two peaks in the strain derivative matches with the corresponding peaks in the capacity derivative within ± 0.02 V. Two peaks in the capacity derivatives correspond to the appearance of intermediate Na_{0.7}FePO₄ during transition of NaFePO₄ phase to FePO₄ phase [6,42,45]. A similar evolution in strain and capacity derivatives is also observed in the earlier desodiation cycles too (Supp. Figure 5). During discharge, two overlapping 2-phase reactions FePO₄ - Na_{2/3}FePO₄ and Na_{2/3}FePO₄ - NaFePO₄ take place in potentials close to each other, therefore they merged into a single plateau with the overlap of the two reactions, leading to 3 phase coexistence at half discharge [42–44]. Our measurements at a slow rate showed that there are almost two capacity and strain

peaks observed during the fourth discharge cycle in 2.80 and 2.84 V, and these peaks were separated with a very narrow potential window.

In general, the electrode experiences reversible and irreversible deformations during Na ion intercalation. The irreversible physical response of the electrodes has been attributed to the formation of cathode – electrolyte interface (CEI), the dissolution of transition metal ions, and the generation of defects in the crystalline structure [4,5]. Reversible deformations in the Na-ion electrodes are correlated with the changing lattice parameters as alkali metal ions are intercalated into and deintercalated from the electrode [27,53]. In the next section, the role of scan rate and intercalation time on the physical response of the sodium iron phosphate electrode is investigated to elaborate these reversible and irreversible changes in the sodium iron phosphate electrode. We will discuss how rate and intercalation time impacts the irreversible behavior of electrode as well as intercalation mechanics.

3.2. Electrochemical Strain Generation at Different C-Rates: NFP cathodes were cycled at C/10, C/4, 1C and 2C scan rates while monitoring in situ strain evolutions in the composite electrode (Supp. Figure 4). Single potential plateaus are observed during the insertion of Na ions at 2.82, 2.68, and 2.44 V for C/10, C/4, and 1C rates, respectively. There was no clear potential plateau observed for the electrode cycled at 2C rate, it is likely due to the low charge / discharge capacity of the electrode when cycled at 2C rate. Discharge capacities in the first cycle were 142, 125, 83.9 and 20.4 mAh g⁻¹ at C/10, C/4, 1C and 2C rates, respectively. Two distinct potential plateaus were clearly observed when the electrode was charged at C/10 and C/4 rates. These two potential plateaus are corresponding to the appearance of intermediate Na_{0.7}FePO₄ during the transition of the NaFePO₄ phase to FePO₄ phase [6,42,45]. However, these potential plateaus became less pronounced in the subsequent cycles when the electrode is cycled at a 1C and 2C rates rate (Supp. Figure 2 and 3). The overpotential is calculated by subtracting a potential at beginning of the first plateau during charge (marked with circle times symbol on the Supp. Figure 4) from the potential at the beginning of the single plateau during discharge (marked with asterisk symbol on the Supp. Figure 4). The overpotential in the first cycle were 0.02, 0.10, 0.27, 0.65 and 1.03V at C/25, C/10, C/4, 1C and 2C rates, respectively. The increase in potential hysteresis at higher scan rates has been observed for other cathode materials during Li and Na intercalation [54,55]. Previous experimental studies, as well as mathematical models also showed the increase in the

overpotential with increasing scan rates [45,56,57]. For sodium, both reaction kinetics and diffusion rates are sluggish compared to lithium. This, in turn, increases the overpotentials required to insert or remove sodium from the FePO_4 structure, especially at higher scan rates.

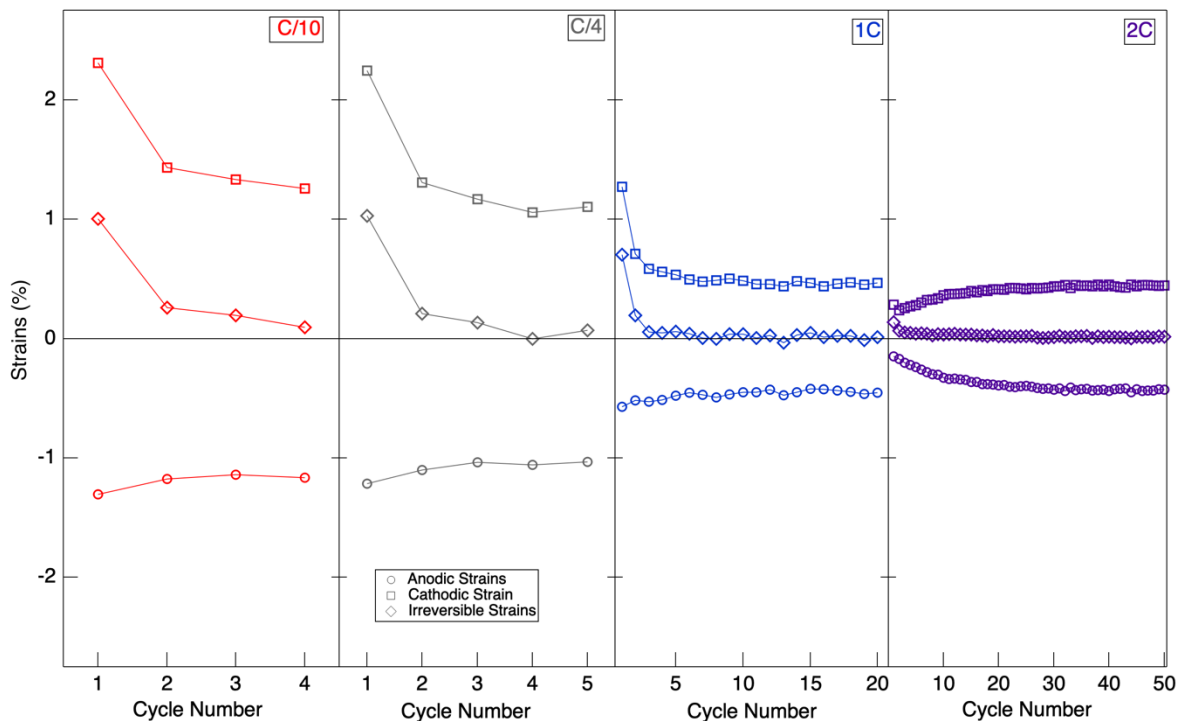


Figure 3: Anodic, cathodic and irreversible strain at C/10 (red color), C/4 (grey color), 1C (blue color) and 2C (purple) rates.

Supp. Figure 4 shows the electrochemical strain evolution in the composite sodium iron phosphate electrode cycled at C/10, C/4, 1C and 2C rates. Electrochemical strains demonstrated a linear relationship with galvanostatic charging / discharging at all different scan rates. The progression of anodic, cathodic, and irreversible strain generation with cycle numbers at different scan rates are plotted in Figure 3. The cathodic strain became 2.31, 2.25, 1.27% and 0.28% at the end of the first discharge cycle at C/10, C/4, 1C and 2C rates, respectively. During the first charge cycle, -1.31, -1.22, -0.57% and -0.15% anodic strains are generated at C/10, C/4, 1C and 2C rates, respectively. In the subsequent cycles, the average anodic strains became -0.46, -1.05, and -1.16% within the margin of 0.02% at C/10, C/4, and 1C rates, respectively. Like C/25 rate, slightly asymmetrical strain evolution in magnitude was detected between charge and discharge cycles when the electrode cycled at C/10. Interestingly, the cathodic and anodic strain increased by the cycle number at 2C rate with cycle number, while irreversible strains was below 0.1%. Irreversible

strains at the end of the first cycle were 1.00, 1.03, 0.70 and 0.13% at C/10, C/4, 1C and 2C rates, respectively. Irreversible strains decreased rapidly in the subsequent cycles. The generated

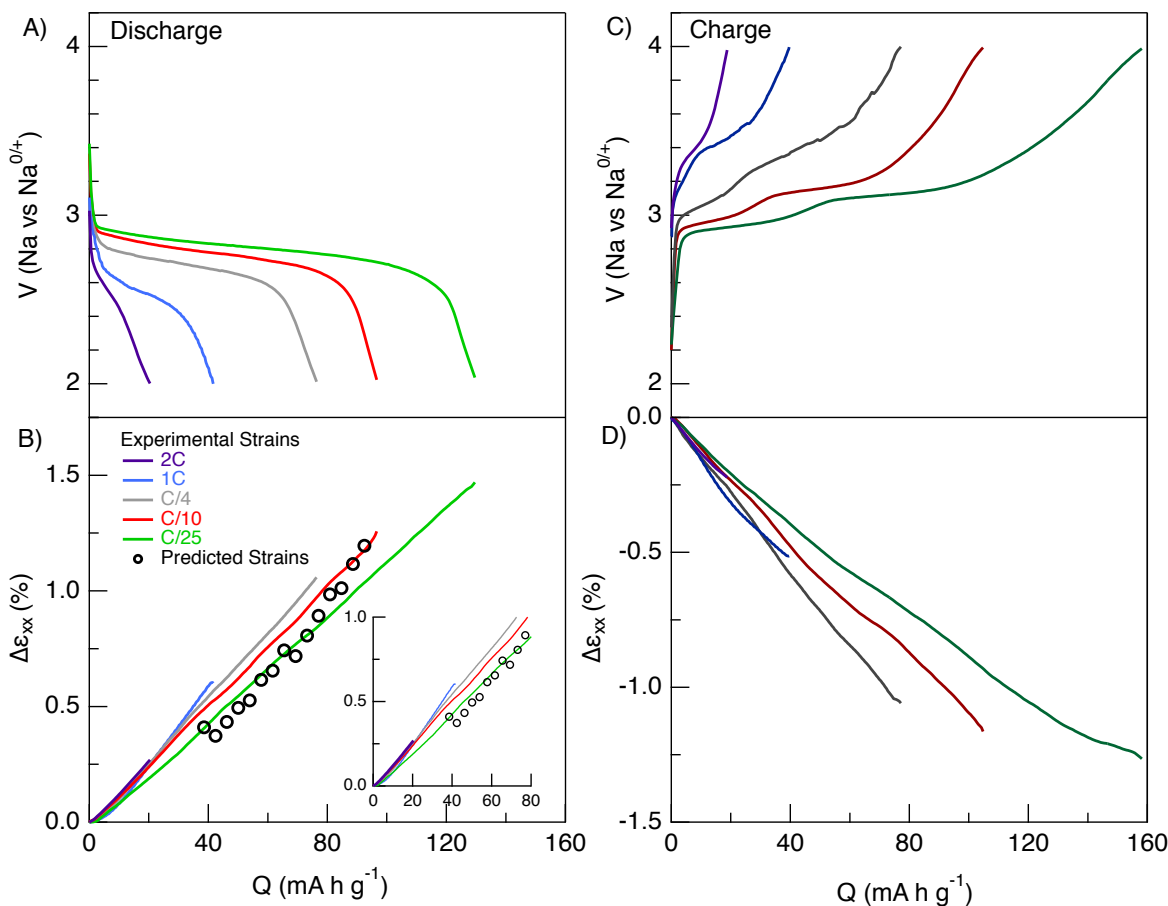


Figure 4: Voltage and strain evolution in iron phosphate composite electrode during sodium intercalation in 1 M NaClO₄ in EC/DMC electrolyte at different scan rates during the 4th cycle. Dotted points indicate the predicted strains calculated from the mathematical model.

irreversible strains in the third cycle were 0.19, 0.13, 0.05% and 0.05% for C/10, C/4, 1C and 2C rates, respectively.

The total amount of sodium ions displaced during cycling directly influences the strain evolution in the electrode. Previous studies on Li-ion electrodes showed a linear relationship between the capacity and strain evolution in graphite anode and lithium manganese oxide cathode materials [49,52]. In situ stress and XRD studies on lithium manganese oxide [58], graphite [59], lithium cobalt oxide [60], and lithium iron phosphate [42] showed the linear relationship between capacity and physical response of electrodes. To better understand the rate-dependent strain generation in the composite sodium iron phosphate cathode, electrochemical strains during the

fourth charge and discharge cycles at different rates are plotted with respect to capacity in Figure 4. Strain values were shifted to zero at the beginning of each charge and discharge cycle to calculate strain generation in each cycle. The strain increases almost linearly with respect to charge and discharge capacities at all scan rates. However, the rate of the electrochemical strains with respect to capacity depends on the applied scan rate. For example, when the sodium ions are intercalated into the electrode until the discharge capacity becomes 40 mAh g^{-1} , the composite electrode expands 0.426, 0.505, 0.540, and 0.589% when cycled at C/25, C/10, C/4, and 1C rates, respectively. The slope of the strains with respect to the state of discharge (SOD) is calculated as 1.75, 1.99, 2.13, 2.04 and 2.25 at C/25, C/10, C/4, 1C and 2C rates, respectively. When considering the same charge capacity, the electrode volume also shrinks greater at faster rates. Strain and capacity relationships during the third cycle are also compared at different scan rates in the Supp. Figure 10. The distinct difference in the electrochemical strain evolution during charge is clearly observed for the third charge cycle too. The magnitude of electrochemical strains was slightly higher at faster rates in the third charge cycle. The electrode experience larger strains at faster scan rates although the same amount of sodium ions is inserted into or extracted from the electrode. However, it is important note that the additional strains at higher rates compared to the slower rates are more pronounced during charge cycles compared to discharge cycles.

Overall, there are two distinct rate-dependent physical responses of the composite NFP electrode. The first one is asymmetrical strain evolution between charge and discharge cycles at slower rates. The electrode demonstrated a more symmetrical strain evolution between charge and discharge rates when cycled at faster rates, which leads to smaller irreversible strain generation in each cycle (Figure 3). Another distinct physical behavior of the electrode is the rate-dependent strains with respect to capacity. When the same amount of sodium is inserted into or removed from the electrode, the electrode undergoes larger volumetric changes at faster rates. To shed light on these discrepancies, we will discuss the possible factors, such as the progression of cathode-electrolyte interface (CEI) formation, and the transport-mechanics coupling of Na ions in the cathode particles, on the rate- and time-dependent electrochemical strains.

3.3. Progression of Irreversible Strains: Irreversible deformations in the electrodes have been attributed to the dissolution of transition metal from the structure of the electrode [61], vacancy formations in the crystalline structure, and the formation of CEI layers [62]. To differentiate these

factors on the irreversible strains at different rates, the cumulative irreversible strains were plotted with respect to cycle number (Figure 5A). If the dominant force on the irreversible deformation is the dissolution of iron metal from the NaFePO_4 structure, we expect to observe negative irreversible strains with increasing cycle numbers. Zhao et. al showed the reduction in strains in lithium manganese oxide cathodes due to the dissolution of manganese into electrolyte [63]. Since

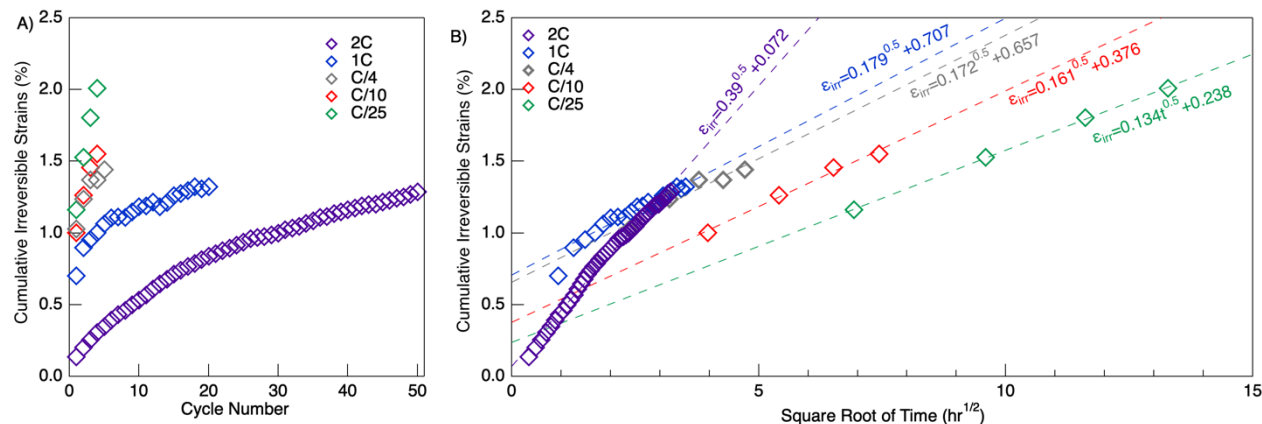


Figure 5: Cumulative irreversible strains in the composite NFP electrode cycled at 2C (purple), 1C (blue), C/4 (grey), C/10 (red), and C/25 (green) rates. The cumulative irreversible strains are plotted with respect to (A) cycle number and (B) square root of cycling time. Dash lines represent the fitted data with the fitted equation.

the cumulative irreversible strains increased with cycle number for all scan rates, it is unlikely that the dissolution of iron dominates the irreversible behavior in the sodium iron phosphate electrode.

Another factor contributing to irreversible deformation could be the formation of vacancies in the crystal structure of the electrode. Unexpected compressive stress generation was observed during the first delithiation cycle in lithium manganese oxide cathode [64] and the irreversible behavior was associated with the formation of oxygen vacancies in the electrode structure. Large irreversible strains were detected in the first cycle of lithium intercalation into lithium iron phosphate and lithium manganese oxide electrodes [47,48]. Figure 5 demonstrates the large deformations only in the first cycle in sodium iron phosphate cathode at all scan rates. Although the generation of oxygen vacancies may contribute to the irreversible behavior of sodium iron phosphate in the first cycle, they are unlikely to cause the progressive evolution of irreversible strains with increasing cycle numbers.

The formation of cathode – electrolyte interface (CEI) layers is a well-known phenomenon causing irreversible deformation in the alkali-metal ion battery electrodes. Oxidation of electrolyte species at high voltages and interaction between electrolyte and cathode can cause the formation of organic and inorganic layers on the cathode surface [4,5]. Smith et al. previously demonstrated

that the thickness of the solid-electrolyte interface layer increases approximately with the square root of time on graphite electrode in Li-ion batteries [65]. Cycle time and operational temperature dominate the solid-electrolyte interface growth rate, not the cycle number [65–67]. Also, a continuum-based mathematical model predicted the growth rate of solid-electrolyte interface layers with the square root of time [68]. Previously, we observed a linear relationship between cumulative irreversible strains and the square root of time for graphite anode and lithium manganese oxide cathodes for Li-ion batteries. The irreversible strains were associated with the electrolyte decomposition on the surface of the electrodes [47,53].

To shed light on irreversible strains on the sodium iron phosphate electrode, the cumulative irreversible strains were plotted against the square root of time (Figure 5B). A linear relationship between cumulative irreversible strain generation and the square root of time is observed for all scan rates. Interestingly, the electrode undergoes larger cumulative irreversible strain generation at faster rates when cycled for the same amount of time. As a result, the rate of irreversible strain with respect to the square root of time increases from $0.134 \text{ hr}^{-0.5}$ at C/25 to $0.179 \text{ hr}^{-0.5}$ at 1C. The slope was calculated as $0.390 \text{ hr}^{-0.5}$ at 2C rate. Attia et al. also demonstrated a similar correlation between the rate of solid electrolyte interface growth and nominal C-rate for Li-ion graphite electrode [69].

If we assume that the growth of CEI layers on the electrode causes an overall increase in the size of the sodium iron phosphate particles, then this deformation on the electrode surface will lead to irreversible macroscopic expansions of the electrode. Based on this assumption, we previously estimated the thickness of the decomposition products for Li-ion graphite composite electrode using the following equation;

$$h_{CEI} = 0.5 D_{particle} \epsilon_{irr} \quad (1)$$

where h_{CEI} , $D_{particle}$, and ϵ_{irr} denote the thickness of the CEI layer, the original size of the particle diameter, and generated irreversible strains, respectively [53]. The average particle size in the composite sodium iron phosphate cathode is about 250 nm. With the given irreversible strains of 1-2% on the electrode, the thickness of the CEI layer is estimated to be ca. 1.25 – 2.5 nm. Previous studies based on X-ray photoelectron spectroscopy detected a few nanometer-thick layer of CEI on lithium iron phosphate and nickel manganese cobalt oxide cathodes [66,70]. Therefore, the estimated thickness of CEI from the strain measurements is consistent with the experimentally measured CEI thickness.

To summarize this section, the irreversible strains increase linearly with the square root of time for all scan rates. This correlation between irreversible deformations and time suggests the contribution of the CEI growth on the irreversible strains. Since the rate of decomposition on the electrode surface is time-dependent, the irreversibility causes asymmetrical strain response between anodic and cathodic cycles at slower rates. The growth of the CEI layer contributes to irreversible positive strain evolution in the electrode. In addition to intercalation-induced strain, if the CEI growth is the only irreversible factor causing strains in the electrode, then it was expected to observe more positive strain generation during sodiation and less negative strains during desodiation at the slower rates, compared to the behavior of electrode cycled at faster rates because of the difference in intercalation time. However, this cannot simply explain the rate-dependent strain profiles observed in Figure 4 and Supp. Figure 10. Local volume mismatch between separated phases in the electrode structure and mismatch strains due to rate-dependent concentration gradients in the electrode might also contribute to the rate-dependent strain behavior. In the following section, we will discuss the factor of diffusion-limitations at faster rates and their impact on the strain evolution in the electrode.

3.4. Predicted Strains in Composite Electrode: A typical composite electrode consists of active materials, conductive carbon, and polymeric binders. Conductive carbon and polymeric binders do not intercalate with ions, their function is to provide conductive network and mechanical strength in the composite electrodes [71,72]. During battery operation, electrochemical strains in the active materials during ion intercalation (e.g. NaFePO₄) governs the volumetric changes in the composite electrode. Previously, the expansions in the Li-ion battery composite electrodes were estimated by considering the volumetric changes in the active particles and calculating the elastic properties of the composite electrode [73,74]. The model assumes that lithium ions are uniformly distributed in the active particles. The model only considers elastic and reversible deformations upon reversible Li⁺ ion intercalation. Also, the impact of side reactions, defect formations, plastic deformations, and the formation of the cathode-electrolyte interface are not included in the model calculation. The individual active materials might show anisotropic behaviors, however, the randomly distributed active materials in the composite network leads to isotropic behaviors in the composite electrodes at the length scales considered in the model. The predicted strains showed good correlations with the experimentally measured composite strains in Li-ion batteries when the

electrodes were cycled at slow scan rates [73,74]. Sodium-intercalation induced strain in the composite NaFePO₄ electrode is calculated by adjusting the previous composite model for Na-ion batteries. Strains in composite electrode, ϵ_{ce} is computed as,

$$\epsilon_{ce} = \epsilon_{NFP} \phi_{NFP} + \left(\frac{\epsilon_{NFP}}{\frac{1}{K_{pm}} - \frac{1}{K_{NFP}}} \right) \left(\frac{1}{K_e} - \frac{1}{K_{average}} \right) \quad (2)$$

Elastic properties of the composite electrode such as bulk modulus, K , are calculated by using open cell theory for anisotropic porous solid end S-combining rule [75]. The volumetric fraction of the NFP particles, ϕ_{NFP} , in the composite electrode is calculated by measuring the porosity of the composite electrode. The model and porosity calculations are described in the supporting information. Calculation of the strains in the composite electrode requires information about the linear strains in the NFP particles, ϵ_{NFP} , during Na⁺ ion intercalation. Changes in the lattice parameters can be used to calculate linear strains in the NFP particles. Previously, Casas-Cabanas and her group intensively investigated the structural changes in the olivine NaFePO₄ during charging / discharging by using synchrotron X-ray diffraction experiments [42–46]. The intensity of the low angle diffraction peaks of the phases, unit cell parameters and cell volumes is plotted with respect to Na content in the electrode discharged at C/66 rate in Supp. Figures 11 and 12 using the previously published XRD study [45].

Linear strain in the sodium iron phosphate electrodes was calculated from the changes in the cell volume of the electrode particles with respect to SOD. The predicted strains in the unconstrained composite electrode are compared with the experimentally measured strains during discharging at different scan rates in Figure 4B. In the calculations, the predicted strains were calculated between SOD of 0.25 – 0.65 to avoid the three-phase region at around 0.65 state of discharge. The corresponding discharge capacity at 0.25 SOD is 38.5 mAh g⁻¹. The predicted strains were shifted by 0.41% to provide a better comparison with the experimentally measured strains. The model predictions resemble the experimentally measured strains at slow scan rates until discharge capacity becomes 80 mAh g⁻¹. Note that the model assumes uniform sodiation of the sodium iron phosphate electrode and it is incapable of incorporating possible mismatch strains associated with large concentration gradients at faster scan rates. We hypothesize that the diffusion-limited concentration profile of Na ions in the electrode particles causes mismatch strains at faster scan rates. To further investigate, we calculate the concentration gradients and mismatch strain profiles in the electrode particle using Fick's law.

3.5. Predicted Na Concentration and Mismatch Strains in the Electrode Particle: An analytical model based on Fick's law and elastic deformation was developed to simulate the concentration profile of Li ions and stress generation in various shapes and orientations of Li-ion battery electrodes [7,32,34,35,76–78]. We adopted previous diffusion-mechanics models of Li-ion batteries into Na-ion batteries to compute the Na concentration gradient and mismatch strains in spherical NaFePO₄ particles. In the olivine NaFePO₄ structure, FeO₆ octahedra connect with neighbor FeO₆ by sharing corner in the ab plane, whereas PO₄ tetrahedra shares corners and edges with the FeO₆ octahedra. The structure provides open channels along the a-axis and b-axis for Na ions. We consider a simple problem of diffusion of Na ions within the sphere shape of particles with the radius, r . From SEM images, the average radius of the particles was around 125 nm. The concentration of sodium in the particle is governed by time-dependent Fick's law [35];

$$\frac{\partial c}{\partial t} = \frac{D}{r^2} \frac{\partial}{\partial r} \left(r^2 \frac{\partial c}{\partial r} \right) \quad (3)$$

The primary driving force for sodium diffusion is the concentration gradient. GITT measurements were performed to calculate the diffusion coefficient of the sodium in the NaFePO₄ particles (Supp. Information). The diffusion coefficient varies between $1 \times 10^{-14} \text{ cm}^2/\text{s}$ and $1 \times 10^{-17} \text{ cm}^2/\text{s}$ during intercalation of Na ions. In the calculations, we assume constant diffusivity of $2 \times 10^{-15} \text{ cm}^2/\text{s}$ and the stress-induced diffusion is neglected. Initial and boundary conditions are given by;

$$C(r, 0) = 0 \text{ for } 0 \leq r \leq R \quad (4)$$

$$D \frac{\partial C(0,t)}{\partial t} = 0 \text{ for } t \geq 0 \quad (5)$$

$$D \frac{\partial C(R,t)}{\partial t} = \frac{I}{F} \text{ for } t \geq 0 \quad (6)$$

At the surface of the electrode, current density, I is constant under galvanostatic discharging and it can be defined with the galvanostatic discharge rate as $I = (C - \text{rate}) \frac{\alpha \rho R}{3}$ where α and ρ denote theoretical capacity and density of the electrode, respectively. The C-rate represents the amount of time it takes to discharge the battery with respect to its theoretical capacity. C_{max} is the maximum concentration of sodium in the NaFePO₄. In Figure 4, the state of discharge at the end of the discharge was 0.27, 0.50, 0.62, and 0.84 when the electrode was cycled at 1C, C/4, C/10, and C/25 rates, respectively. To simulate the concentration gradients and mismatch strains, the electrode particles are discharged until the average SOD in the particle

reached the experimentally observed SOD for four different scan rates in Figure 1 and the Supp. Figure 4. As a reference point, the concentration profile of sodium is also computed when cycled at C/100 until 0.95 SOD. The concentration profile of sodium inside the electrode particles is estimated by solving the partial differential diffusion equation using the MATLAB PDEPE toolbox.

Figure 6 shows the distribution of sodium at different C-rates. At slower rates (C/100 and C/25), sodium is almost uniformly distributed along the particle radius. When the scan rate increased further, the concentration of sodium near the particle surface differs significantly from the concentration in the center of the particles. As a result, a large sodium concentration gradient is observed near the electrode surface at faster rates. We calculate the deformation mismatch due to the

inhomogeneous distribution of sodium inside the electrode particle by following the previous elastic model developed for Li-ion batteries [32]. Mismatch strains are calculated as

$$\varepsilon(r) = \frac{l(r) - l|_{r=0}}{l|_{r=0}} \quad (7)$$

Concentration dependent-lattice parameters among the a-axis and b-axis are used to calculate strains. Shortly, the estimated concentration profiles throughout the radius of the electrode particle were converted into radius and time-dependent SOD and match with the lattice parameter in the a-axis and b-axis from the Supp. Figure 11. Steep concentration gradients at faster scan rates result in the generation of large mismatch strains in the electrode particle.

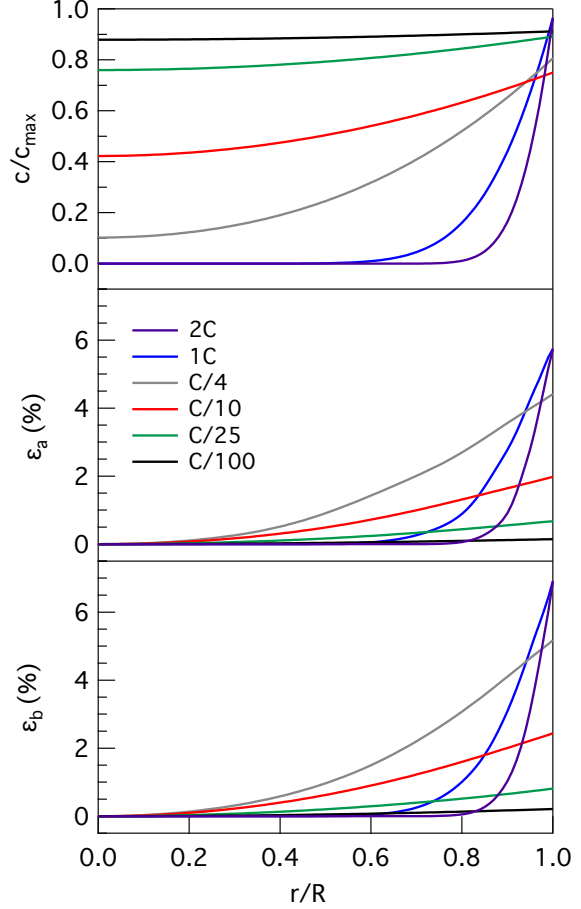


Figure 6: Na Concentration and Mismatch Strains in Electrode Particle: The sodium concentration profiles and the mismatch strains at five different scan rates. In the calculations, it is assumed that the electrode particles are discharged until 0.15, 0.27, 0.50, 0.62, 0.84 and 0.9% state of discharge for 2C, 1C, C/4, C/10, C/25 and C/100. The state of discharge values for each rate is chosen based on experimentally measured electrode capacity in Figure 5.

The average concentration in the electrode particle (\bar{C}_{ave} , where $\bar{C}_{ave} = C/C_{max}$), average mismatch strains in the particle along a-axis ($\varepsilon_{a,ave}$) and b-axis ($\varepsilon_{b,ave}$) are calculated from the simulation and tabulated in Table 1. Average values are calculated via $\Phi_{ave} = \frac{\int_0^R \Phi dr}{\int_0^R dr}$ where $\Phi = \bar{C}_{ave}, \varepsilon_a$ or ε_b . Average predicted Na concentrations in the electrode particle at different rates are in good agreement with the experimentally measured Na content in the composite electrode (Figure 4). The average mismatch strain evolution per charge is greater in magnitude when the electrode is cycled at faster rates. These mismatch strains in the electrode particle leads to additional macroscopic expansions of the composite electrode at faster rates.

Table 1: Average concentration in the electrode particle \bar{C}_{ave} , and mismatch strains in the particle along a-axis ($\varepsilon_{a,ave}$) and b-axis ($\varepsilon_{b,ave}$).

C-rates	2C	1C	C/4	C/10	C/25	C/100
\bar{C}_{ave}	0.15	0.30	0.53	0.63	0.84	0.89
$\varepsilon_{a,ave} / \bar{C}_{ave}$	6.17	6.19	5.21	2.08	0.53	0.10
$\varepsilon_{b,ave} / \bar{C}_{ave}$	6.91	7.00	5.95	2.55	0.63	0.14

3.6. Factors Contribution Electrochemical Strains in NaFePO₄ Electrode: Intercalation of Na ions generates electrochemical strain generation in the composite electrode (Figure 1). Strain derivatives during charge / discharge cycles match well with the capacity derivatives, which points out that the phase transformation in the electrode causes potential-dependent strain rate changes in the electrode (Figure 2). Strains also show very linear dependence on the capacity. Predicted composite strains based on anisotropic porous solid end S-combining rule also agrees well with the electrochemically measured strains at C/25 rate (Figure 4). The measurements also point out to irreversible and rate-dependent strain generation factors in the electrode in addition to the intercalation-induced electrochemical strains. First, large amount of irreversible strain generations is detected in the early cycle (Figure 3). Cumulative irreversible strain shows a linear dependence with the square root of the cycle time (Figure 5). When irreversible strain generation becomes negligible small in the subsequent cycles compared to the intercalation-induced strains, the electrode experiences a slightly larger expansion when cycled at the faster rate (Figure 4). This behavior suggests the rate-dependent strain evolution in the composite electrode. In summary, strains in the composite sodium iron phosphate electrode, ε_c can be defined as

$$\varepsilon_c = \varepsilon_i(Q) + \varepsilon_M(v) + \varepsilon_{\Delta-phase} + \varepsilon_{CEI}(t) + \varepsilon_{other} \quad (8)$$

where $\varepsilon_i(Q)$ is the capacity-dependent intercalation-induced strains, $\varepsilon_M(v)$ is the rate-dependent mismatch strains due to concentration gradients, $\varepsilon_{\Delta-phase}$ is mismatch strains due to the volume mismatch between separated phases in the electrode structure, $\varepsilon_{CEI}(t)$ is time-dependent, CEI-induced irreversible strains. ε_{other} is the strain generation due to the combination of other irreversible deformations such as oxygen vacancies, dissolution of iron, and irreversible structural or microstructural changes (e.g. cracks). Experimentally measured and predicted composite strains in Figure 4 indicate the linear relationship between intercalation-induced strains, $\varepsilon_i(Q)$ and the electrode capacity. Time-dependent cumulative irreversible strains in Figure 5 points out the contribution of CEI growth on the irreversible deformation, $\varepsilon_{CEI}(t)$. Large irreversible strains are detected during the first cycle at any scan rates (Figure 1 and Supp. Figure 4) and it can be associated with either $\varepsilon_{CEI}(t)$ and/or ε_{other} .

Rate-dependent strain rates with respect to capacity in Figure 6 is associated with the generation of mismatch strains in the electrode. Mismatch strains, $\varepsilon_M(v)$, can be generated due to rate-dependent concentration gradients in the electrode particle and volume mismatch between two separate phases in the electrode. The energy accommodation during mechanical deformations in the electrode widens the potential gap between the electrochemical redox reactions, which leads to higher potential hysteresis [62]. Zhu and Wang calculated the strain accommodation energy for LiFePO₄ electrodes with 40-nm and 100-nm particle sizes. The bigger particles require large potential hysteresis to accommodate the volume differences between Li-rich and Li-poor phases [79]. Synchrotron X-ray diffraction and pair distribution function analysis suggest NaFePO₄ accommodates discontinuous volume changes in the electrode by forming short-range amorphous phases [6]. Operando synchrotron study also suggested the formation of mismatch strains on NaFePO₄ cathodes induces cost of mechanical energy, which causes larger potential hysteresis between redox reactions [80]. The analytical model predicted sharper concentration gradients and localized strain generation near the electrode surface during Li-ion intercalation electrode [32–38]. In situ stress measurements and finite strain model demonstrated local stress gradients near the Si thin film electrode surface due to sharp concentration gradients near surface [81,82]. In our study, the transport model only simulates the rate-induced concentration gradient within the solid solution (Figure 6). The model predicts sharp concentration gradients of Na near the electrode surface at higher rates, which contributes to greater mismatch strains (Table 1). It should be noted that large

concentration gradients impede the volume mismatch between two separate phases in the electrode. Although predicted strain values do not incorporate the phase separation factor, it demonstrates the contribution of sharp concentration gradients at faster rates on the mismatch strains.

4. CONCLUSION

A better understanding of the rate effect on electrode mechanics is required to develop new electrodes with better rate-capabilities. In this work, we interrogated the impact of scan rate on electrochemical strain generations in the NaFePO₄ composite cathode for Na-ion batteries. Digital image correlation was used to monitor strain generation in the composite cathode during cycling at different scan rates. A large irreversible strain is observed in the first cycle at all scan rates. A linear relationship between electrode capacity and strain evolution is observed at all scan rates. Asymmetrical strain evolution between anodic and cathodic cycles is observed at slower rates and it was attributed to the generation of time-dependent irreversible strains due to CEI growth. The rate of increase in the cumulative irreversible strain was greater when the electrode cycled at faster rates. The remarkably larger intercalation-induced strain evolution is observed in the composite electrode when cycled at faster scan rates. Experimental strain measurements were compared with the predictions from an analytical model for composite electrodes based on uniform elastic deformations and intercalation-induced structural changes in the NFP particles. A transport-mechanics model is developed to predict the concentration profile of Na in the electrode particles and associated mismatch strains at different scan rates. Our study demonstrated the scan rate-dependent and time-dependent additional volumetric changes in the electrode due to the formation of CEI layers and mismatch strains. When considering commercial electrodes being constrained by current collectors and battery packing, these constrained electrodes will be more prone to mechanical degradations at faster rates due to larger electrochemical strains. Mechanical instabilities in the electrode particles will shorten the lifetime and worsen the performance of the battery electrodes.

Author Contributions: The manuscript was written through the contributions of all authors. All authors have given approval to the final version of the manuscript. H. Dykes and B. Özdogru contributed equally. Ö. Ö. Ç. conceived the idea and supervised the work. B. Ö. performed in situ

strain measurements and impedance spectroscopy, H. D. compiled analytical model and D. G. performed GITT measurements. D. S and M.C. C. provided XRD analysis from their previously published paper. All authors discussed the results. All data needed to evaluate the conclusions in the paper are present in the paper and/or the Supporting information. Additional data related to this paper may be requested from the authors.

Declaration of competing interest: The authors declare that they have no known competing financial interests or personal relationships that could have appeared to influence the work reported in this paper.

Acknowledgments: This work was supported by the U.S. Department of Energy, Office of Science, Basic Energy Sciences (Award number DE-SC0021251). The in situ strain measurements and the development of analytical model were supported by DOE Office of Basic Science. All in situ strain measurement and impedance spectroscopy measurements were carried out at Oklahoma State University. MCC and DS are grateful to the Basque Government through the Elkartek grants CICE2019 and CICE2020 (KK 2020/00078), to Ministerio de Economía y Competitividad through NIB-MOVE grant (PID2019-107468RB-C22). VM acknowledges funding as part of the Joint Center for Energy Storage Research, an Energy Innovation Hub funded by the U.S. Department of Energy, Office of Science, Basic Energy Science.

REFERENCES

- [1] M. Li, J. Lu, Z. Chen, K. Amine, 30 Years of Lithium-Ion Batteries, *Adv. Mater.* 30 (2018) 1–24. <https://doi.org/10.1002/adma.201800561>.
- [2] G. Berckmans, M. Messagie, J. Smekens, N. Omar, L. Vanhaverbeke, J. Van Mierlo, Cost projection of state of the art lithium-ion batteries for electric vehicles up to 2030, *Energies*. 10 (2017). <https://doi.org/10.3390/en10091314>.
- [3] M.D. Slater, D. Kim, E. Lee, C.S. Johnson, Sodium-ion batteries, *Adv. Funct. Mater.* 23 (2013) 947–958. <https://doi.org/10.1002/adfm.201200691>.
- [4] K. Kubota, M. Dahbi, T. Hosaka, S. Kumakura, S. Komaba, Towards K-Ion and Na-Ion Batteries as “Beyond Li-Ion,” *Chem. Rec.* 18 (2018) 459–479. <https://doi.org/10.1002/tcr.201700057>.
- [5] J. Song, B. Xiao, Y. Lin, K. Xu, X. Li, Interphases in Sodium-Ion Batteries, *Adv. Energy Mater.* 8 (2018). <https://doi.org/10.1002/aenm.201703082>.
- [6] K. Xiang, W. Xing, D.B. Ravnsbæk, L. Hong, M. Tang, Z. Li, K.M. Wiaderek, O.J. Borkiewicz, K.W. Chapman, P.J. Chupas, Y.M. Chiang, Accommodating High Transformation Strains in Battery Electrodes via the Formation of Nanoscale Intermediate Phases: Operando Investigation of Olivine NaFePO₄, *Nano Lett.* 17 (2017) 1696–1702. <https://doi.org/10.1021/acs.nanolett.6b04971>.
- [7] K. Zhao, M. Pharr, S. Cai, J.J. Vlassak, Z. Suo, Large plastic deformation in high-capacity lithium-ion batteries caused by charge and discharge, *J. Am. Ceram. Soc.* 94 (2011) s226–s235. <https://doi.org/10.1111/j.1551-2916.2011.04432.x>.
- [8] M.R. Bonilla, A. Lozano, B. Escribano, J. Carrasco, E. Akhmatkaya, Revealing the Mechanism of Sodium Diffusion in Na_xFePO₄ Using an Improved Force Field, *J. Phys. Chem. C*. 122 (2018) 8065–8075. <https://doi.org/10.1021/acs.jpcc.8b00230>.
- [9] C.M. Wang, X. Li, Z. Wang, W. Xu, J. Liu, F. Gao, L. Kovarik, J.G. Zhang, J. Howe, D.J. Burton, Z. Liu, X. Xiao, S. Thevuthasan, D.R. Baer, In situ TEM investigation of congruent phase transition and structural evolution of nanostructured silicon/carbon anode for lithium ion batteries, *Nano Lett.* 12 (2012) 1624–1632. <https://doi.org/10.1021/nl204559u>.
- [10] M. Gu, Y. Li, X. Li, S. Hu, X. Zhang, W. Xu, S. Thevuthasan, D.R. Baer, J.G. Zhang, J. Liu, C. Wang, In situ TEM study of lithiation behavior of silicon nanoparticles attached to

- and embedded in a carbon matrix, *ACS Nano*. 6 (2012) 8439–8447. <https://doi.org/10.1021/nn303312m>.
- [11] X.H. Liu, Y. Liu, A. Kushima, S. Zhang, T. Zhu, J. Li, J.Y. Huang, In situ TEM experiments of electrochemical lithiation and delithiation of individual nanostructures, *Adv. Energy Mater.* 2 (2012) 722–741. <https://doi.org/10.1002/aenm.201200024>.
- [12] H. Xie, X. Tan, E.J. Lubner, B.C. Olsen, W.P. Kalisvaart, K.L. Jungjohann, D. Mitlin, J.M. Buriak, β -SnSb for Sodium Ion Battery Anodes: Phase Transformations Responsible for Enhanced Cycling Stability Revealed by in Situ TEM, *ACS Energy Lett.* 3 (2018) 1670–1676. <https://doi.org/10.1021/acseenergylett.8b00762>.
- [13] X. Lu, E.R. Adkins, Y. He, L. Zhong, L. Luo, S.X. Mao, C.M. Wang, B.A. Korgel, Germanium as a Sodium Ion Battery Material: In Situ TEM Reveals Fast Sodiation Kinetics with High Capacity, *Chem. Mater.* 28 (2016) 1236–1242. <https://doi.org/10.1021/acs.chemmater.6b00200>.
- [14] Z. Yang, J. Sun, Y. Ni, Z. Zhao, J. Bao, S. Chen, Facile synthesis and in situ transmission electron microscopy investigation of a highly stable Sb₂Te₃/C nanocomposite for sodium-ion batteries, *Energy Storage Mater.* 9 (2017) 214–220. <https://doi.org/10.1016/j.ensm.2017.07.010>.
- [15] W. Xia, F. Xu, C. Zhu, H.L. Xin, Q. Xu, P. Sun, L. Sun, Probing microstructure and phase evolution of α -MoO₃ nanobelts for sodium-ion batteries by in situ transmission electron microscopy, *Nano Energy*. 27 (2016) 447–456. <https://doi.org/10.1016/j.nanoen.2016.07.017>.
- [16] X. Wang, Z. Yao, S. Hwang, Y. Pan, H. Dong, M. Fu, N. Li, K. Sun, H. Gan, Y. Yao, A. Aspuru-Guzik, Q. Xu, D. Su, In Situ Electron Microscopy Investigation of Sodiation of Titanium Disulfide Nanoflakes, *ACS Nano*. 13 (2019) 9421–9430. <https://doi.org/10.1021/acsnano.9b04222>.
- [17] A. Tokranov, B.W. Sheldon, C. Li, S. Minne, X. Xiao, In situ atomic force microscopy study of initial solid electrolyte interphase formation on silicon electrodes for Li-ion batteries, *ACS Appl. Mater. Interfaces*. 6 (2014) 6672–6686. <https://doi.org/10.1021/am500363t>.
- [18] D.E. Demirocak, B. Bhushan, In situ atomic force microscopy analysis of morphology and particle size changes in Lithium Iron Phosphate cathode during discharge, *J. Colloid*

- Interface Sci. 423 (2014) 151–157. <https://doi.org/10.1016/j.jcis.2014.02.035>.
- [19] J. Park, S. Kalnaus, S. Han, Y.K. Lee, G.B. Less, N.J. Dudney, C. Daniel, A.M. Sastry, In situ atomic force microscopy studies on lithium (de)intercalation-induced morphology changes in Li_xCoO_2 micro-machined thin film electrodes, *J. Power Sources*. 222 (2013) 417–425. <https://doi.org/10.1016/j.jpowsour.2012.09.017>.
- [20] S.D. Lacey, J. Wan, A.V.W. Cresce, S.M. Russell, J. Dai, W. Bao, K. Xu, L. Hu, Atomic force microscopy studies on molybdenum disulfide flakes as sodium-ion anodes, *Nano Lett.* 15 (2015) 1018–1024. <https://doi.org/10.1021/nl503871s>.
- [21] M. Han, C. Zhu, Q. Zhao, C. Chen, Z. Tao, W. Xie, F. Cheng, J. Chen, In Situ Atomic Force Microscopic Studies of Single Tin Nanoparticle: Sodiation and Desodiation in Liquid Electrolyte, *ACS Appl. Mater. Interfaces*. 9 (2017) 28620–28626. <https://doi.org/10.1021/acsami.7b08870>.
- [22] J. Wang, C. Eng, Y.C.K. Chen-Wiegart, J. Wang, Probing three-dimensional sodiation-desodiation equilibrium in sodium-ion batteries by in situ hard X-ray nanotomography, *Nat. Commun.* 6 (2015) 1–9. <https://doi.org/10.1038/ncomms8496>.
- [23] X. Ou, X. Liang, F. Zheng, P. Wu, Q. Pan, X. Xiong, C. Yang, M. Liu, In situ X-ray diffraction investigation of CoSe_2 anode for Na-ion storage: Effect of cut-off voltage on cycling stability, *Electrochim. Acta*. 258 (2017) 1387–1396. <https://doi.org/10.1016/j.electacta.2017.11.198>.
- [24] E. Talaie, V. Duffort, H.L. Smith, B. Fultz, L.F. Nazar, Structure of the high voltage phase of layered $\text{P}_2\text{-Na}_{2/3-z}[\text{Mn}_{1/2}\text{Fe}_{1/2}]\text{O}_2$ and the positive effect of Ni substitution on its stability, *Energy Environ. Sci.* 8 (2015) 2512–2523. <https://doi.org/10.1039/c5ee01365h>.
- [25] M. Li, Z. Wang, J. Fu, K. Ma, E. Detsi, In situ electrochemical dilatometry study of capacity fading in nanoporous Ge-based Na-ion battery anodes, *Scr. Mater.* 164 (2019) 52–56. <https://doi.org/10.1016/j.scriptamat.2019.01.030>.
- [26] N. Karimi, A. Varzi, S. Passerini, A comprehensive insight into the volumetric response of graphite electrodes upon sodium co-intercalation in ether-based electrolytes, *Electrochim. Acta*. 304 (2019) 474–486. <https://doi.org/10.1016/j.electacta.2019.03.036>.
- [27] B. Özdogru, H. Dykes, S. Padwal, S. Harimkar, Ö. Çapraz, Electrochemical strain evolution in iron phosphate composite cathodes during lithium and sodium ion intercalation, *Electrochim. Acta*. 353 (2020). <https://doi.org/10.1016/j.electacta.2020.136594>.

- [28] E.M.C. Jones, M.N. Silberstein, S.R. White, N.R. Sottos, In Situ Measurements of Strains in Composite Battery Electrodes during Electrochemical Cycling, *Exp. Mech.* 54 (2014) 971–985. <https://doi.org/10.1007/s11340-014-9873-3>.
- [29] J. Wang, Y.C.K. Chen-Wiegart, J. Wang, In operando tracking phase transformation evolution of lithium iron phosphate with hard X-ray microscopy, *Nat. Commun.* 5 (2014) 1–10. <https://doi.org/10.1038/ncomms5570>.
- [30] H. Tavassol, M.K.Y. Chan, M.G. Catarello, J. Greeley, D.G. Cahill, A.A. Gewirth, Surface Coverage and SEI Induced Electrochemical Surface Stress Changes during Li Deposition in a Model System for Li-Ion Battery Anodes, *J. Electrochem. Soc.* 160 (2013) A888–A896. <https://doi.org/10.1149/2.068306jes>.
- [31] Ö.Ö. Çapraz, K.R. Hebert, P. Shrotriya, In Situ Stress Measurement During Aluminum Anodizing Using Phase-Shifting Curvature Interferometry, *J. Electrochem. Soc.* 160 (2013) D501–D506. <https://doi.org/10.1149/2.025311jes>.
- [32] K. Zhao, M. Pharr, J.J. Vlassak, Z. Suo, Fracture of electrodes in lithium-ion batteries caused by fast charging, *J. Appl. Phys.* 108 (2010) 073517. <https://doi.org/10.1063/1.3492617>.
- [33] Y.T. Cheng, M.W. Verbrugge, The influence of surface mechanics on diffusion induced stresses within spherical nanoparticles, *J. Appl. Phys.* 104 (2008). <https://doi.org/10.1063/1.3000442>.
- [34] Y.-T. Cheng, M.W. Verbrugge, Diffusion-Induced Stress, Interfacial Charge Transfer, and Criteria for Avoiding Crack Initiation of Electrode Particles, *J. Electrochem. Soc.* 157 (2010) A508. <https://doi.org/10.1149/1.3298892>.
- [35] Y.T. Cheng, M.W. Verbrugge, Evolution of stress within a spherical insertion electrode particle under potentiostatic and galvanostatic operation, *J. Power Sources.* 190 (2009) 453–460. <https://doi.org/10.1016/j.jpowsour.2009.01.021>.
- [36] J. Christensen, J. Newman, A Mathematical Model of Stress Generation and Fracture in Lithium Manganese Oxide, *J. Electrochem. Soc.* 153 (2006) A1019. <https://doi.org/10.1149/1.2185287>.
- [37] J. Christensen, J. Newman, Stress generation and fracture in lithium insertion materials, *J. Solid State Electrochem.* 10 (2006) 293–319. <https://doi.org/10.1007/s10008-006-0095-1>.
- [38] G. Li, C.W. Monroe, Annual Review of Chemical and Biomolecular Engineering

- Multiscale Lithium-Battery Modeling from Materials to Cells, (2020). <https://doi.org/10.1146/annurev-chembioeng>.
- [39] J. Chen, A.K. Thapa, T.A. Berfield, In-situ characterization of strain in lithium battery working electrodes, *J. Power Sources*. 271 (2014) 406–413. <https://doi.org/10.1016/j.jpowsour.2014.08.035>.
- [40] C. Heubner, S. Heiden, B. Matthey, M. Schneider, A. Michaelis, Sodiation vs. Lithiation of FePO₄: A comparative kinetic study, *Electrochim. Acta*. 216 (2016) 412–419. <https://doi.org/10.1016/j.electacta.2016.09.041>.
- [41] C. Heubner, S. Heiden, M. Schneider, A. Michaelis, In-situ preparation and electrochemical characterization of submicron sized NaFePO₄ cathode material for sodium-ion batteries, *Electrochim. Acta*. 233 (2017) 78–84. <https://doi.org/10.1016/j.electacta.2017.02.107>.
- [42] M. Galceran, D. Saurel, B. Acebedo, V. V. Roddatis, E. Martin, T. Rojo, M. Casas-Cabanas, The mechanism of NaFePO₄ (de)sodiation determined by in situ X-ray diffraction, *Phys. Chem. Chem. Phys.* 16 (2014) 8837–8842. <https://doi.org/10.1039/c4cp01089b>.
- [43] M. Casas-Cabanas, V. V. Roddatis, D. Saurel, P. Kubiak, J. Carretero-González, V. Palomares, P. Serras, T. Rojo, Crystal chemistry of Na insertion/deinsertion in FePO₄-NaFePO₄, *J. Mater. Chem.* 22 (2012) 17421–17423. <https://doi.org/10.1039/c2jm33639a>.
- [44] A. Saracibar, J. Carrasco, D. Saurel, M. Galceran, B. Acebedo, H. Anne, M. Lepoitevin, T. Rojo, M. Casas Cabanas, Investigation of sodium insertion-extraction in olivine Na_xFePO₄ ($0 \leq x \leq 1$) using first-principles calculations, *Phys. Chem. Chem. Phys.* 18 (2016) 13045–13051. <https://doi.org/10.1039/c6cp00762g>.
- [45] D. Saurel, M. Galceran, M. Reynaud, H. Anne, M. Casas-Cabanas, Rate dependence of the reaction mechanism in olivine NaFePO₄ Na-ion cathode material, *Int. J. Energy Res.* 42 (2018) 3258–3265. <https://doi.org/10.1002/er.4078>.
- [46] M. Galceran, V. Roddatis, F.J. Zúñiga, J.M. Pérez-Mato, B. Acebedo, R. Arenal, I. Peral, T. Rojo, M. Casas-Cabanas, Na-vacancy and charge ordering in Na_{2/3}FePO₄, *Chem. Mater.* 26 (2014) 3289–3294. <https://doi.org/10.1021/cm501110v>.
- [47] Çapraz, S. Rajput, S. White, N.R. Sottos, Strain Evolution in Lithium Manganese Oxide Electrodes, *Exp. Mech.* 58 (2018) 561–571. <https://doi.org/10.1007/s11340-018-0381-8>.
- [48] B. Ozdogru, H. Dykes, Ö.Ö. Capraz, Electrochemical Strain Evolution in Iron Phosphate Cathode Upon Sodium and Lithium Intercalation, in: 2020 Batteries Gordon Research

- Conference, Ventura, CA, 2020.
- [49] Ö.Ö. Çapraz, S. Rajput, K.L. Bassett, A.A. Gewirth, S.R. White, N.R. Sottos, Controlling Expansion in Lithium Manganese Oxide Composite Electrodes via Surface Modification, *J. Electrochem. Soc.* 166 (2019) A2357–A2362. <https://doi.org/10.1149/2.0021912jes>.
- [50] K.L. Bassett, Ö. Özgür Çapraz, B. Özdogru, A.A. Gewirth, N.R. Sottos, Cathode/Electrolyte Interface-Dependent Changes in Stress and Strain in Lithium Iron Phosphate Composite Cathodes, *J. Electrochem. Soc.* 166 (2019) A2707–A2714. <https://doi.org/10.1149/2.1391912jes>.
- [51] Ö.Ö. Çapraz, K.L. Bassett, A.A. Gewirth, N.R. Sottos, Electrochemical Stiffness Changes in Lithium Manganese Oxide Electrodes, *Adv. Energy Mater.* 7 (2017) 1601778. <https://doi.org/10.1002/aenm.201601778>.
- [52] H. Tavassol, E.M.C. Jones, N.R. Sottos, A.A. Gewirth, Electrochemical stiffness in lithium-ion batteries, *Nat. Mater.* 15 (2016) 1182–1188. <https://doi.org/10.1038/nmat4708>.
- [53] E.M.C. Jones, Ö.Ö. Çapraz, S.R. White, N.R. Sottos, Reversible and Irreversible Deformation Mechanisms of Composite Graphite Electrodes in Lithium-Ion Batteries, *J. Electrochem. Soc.* 163 (2016) A1965–A1974. <https://doi.org/10.1149/2.0751609jes>.
- [54] B. Lu, Y. Song, Q. Zhang, J. Pan, Y.T. Cheng, J. Zhang, Voltage hysteresis of lithium ion batteries caused by mechanical stress, *Phys. Chem. Chem. Phys.* 18 (2016) 4721–4727. <https://doi.org/10.1039/c5cp06179b>.
- [55] D. Eum, B. Kim, S.J. Kim, H. Park, J. Wu, S.P. Cho, G. Yoon, M.H. Lee, S.K. Jung, W. Yang, W.M. Seong, K. Ku, O. Tamwattana, S.K. Park, I. Hwang, K. Kang, Voltage decay and redox asymmetry mitigation by reversible cation migration in lithium-rich layered oxide electrodes, *Nat. Mater.* 19 (2020) 419–427. <https://doi.org/10.1038/s41563-019-0572-4>.
- [56] V. Srinivasan, J. Newman, Discharge Model for the Lithium Iron-Phosphate Electrode, *J. Electrochem. Soc.* 151 (2004) A1517. <https://doi.org/10.1149/1.1785012>.
- [57] Y. Zhu, Y. Xu, Y. Liu, C. Luo, C. Wang, Comparison of electrochemical performances of olivine NaFePO₄ in sodium-ion batteries and olivine LiFePO₄ in lithium-ion batteries, *Nanoscale*. 5 (2013) 780–787. <https://doi.org/10.1039/c2nr32758a>.
- [58] J. Sheth, N.K. Karan, D.P. Abraham, C.C. Nguyen, B.L. Lucht, B.W. Sheldon, P.R. Guduru, In Situ Stress Evolution in Li_{1+x}Mn₂O₄ Thin Films during Electrochemical Cycling in Li-Ion Cells, *J. Electrochem. Soc.* 163 (2016) A2524–A2530.

- <https://doi.org/10.1149/2.0161613jes>.
- [59] A. Mukhopadhyay, A. Tokranov, K. Sena, X. Xiao, B.W. Sheldon, Thin film graphite electrodes with low stress generation during Li-intercalation, *Carbon N. Y.* 49 (2011) 2742–2749. <https://doi.org/10.1016/j.carbon.2011.02.067>.
- [60] S. Il Pyun, J.Y. Go, T.S. Jang, An investigation of intercalation-induced stresses generated during lithium transport through $\text{Li}_{1-\delta}\text{CoO}_2$ film electrode using a laser beam deflection method, *Electrochim. Acta.* 49 (2004) 4477–4486. <https://doi.org/10.1016/j.electacta.2004.05.004>.
- [61] N. Iltchev, Y. Chen, S. Okada, J.I. Yamaki, LiFePO_4 storage at room and elevated temperatures, in: *J. Power Sources*, 2003: pp. 749–754. [https://doi.org/10.1016/S0378-7753\(03\)00215-5](https://doi.org/10.1016/S0378-7753(03)00215-5).
- [62] A. Mukhopadhyay, B.W. Sheldon, Deformation and stress in electrode materials for Li-ion batteries, *Prog. Mater. Sci.* 63 (2014) 58–116. <https://doi.org/10.1016/J.PMATSCI.2014.02.001>.
- [63] L. Zhao, Self-reporting of Mn ion dissolution and self-stabilization of cathode-electrolyte interface in lithium ion batteries, University of Illinois at Urbana Champaign, 2020.
- [64] J. Sheth, N.K. Karan, D.P. Abraham, C.C. Nguyen, B.L. Lucht, B.W. Sheldon, P.R. Guduru, In Situ Stress Evolution in $\text{Li}_{1+x}\text{Mn}_2\text{O}_4$ Thin Films during Electrochemical Cycling in Li-Ion Cells, *J. Electrochem. Soc.* 163 (2016) A2524–A2530. <https://doi.org/10.1149/2.0161613jes>.
- [65] A.J. Smith, J.C. Burns, X. Zhao, D. Xiong, J.R. Dahn, A High Precision Coulometry Study of the SEI Growth in Li/Graphite Cells, *J. Electrochem. Soc.* 158 (2011) A447. <https://doi.org/10.1149/1.3557892>.
- [66] Y. Qian, P. Niehoff, M. Börner, M. Grützke, X. Mönnighoff, P. Behrends, S. Nowak, M. Winter, F.M. Schappacher, Influence of electrolyte additives on the cathode electrolyte interphase (CEI) formation on $\text{LiNi}_{1/3}\text{Mn}_{1/3}\text{Co}_{1/3}\text{O}_2$ in half cells with Li metal counter electrode, *J. Power Sources.* 329 (2016) 31–40. <https://doi.org/10.1016/j.jpowsour.2016.08.023>.
- [67] A. Wang, S. Kadam, H. Li, S. Shi, Y. Qi, Review on modeling of the anode solid electrolyte interphase (SEI) for lithium-ion batteries, *Npj Comput. Mater.* 4 (2018). <https://doi.org/10.1038/s41524-018-0064-0>.

- [68] H.J. Ploehn, P. Ramadass, R.E. White, Solvent Diffusion Model for Aging of Lithium-Ion Battery Cells, *J. Electrochem. Soc.* 151 (2004) A456. <https://doi.org/10.1149/1.1644601>.
- [69] P.M. Attia, S. Das, S.J. Harris, M.Z. Bazant, W.C. Chueh, Electrochemical kinetics of SEI growth on carbon black I: Experiments, *ArXiv.* (2019). <https://doi.org/10.1149/2.0231904jes>.
- [70] S. Malmgren, K. Ciosek, M. Hahlin, T. Gustafsson, M. Gorgoi, H. Rensmo, K. Edström, Comparing anode and cathode electrode/electrolyte interface composition and morphology using soft and hard X-ray photoelectron spectroscopy, *Electrochim. Acta.* 97 (2013) 23–32. <https://doi.org/10.1016/j.electacta.2013.03.010>.
- [71] H. Zheng, R. Yang, G. Liu, X. Song, V.S. Battaglia, Cooperation between active material, polymeric binder and conductive carbon additive in lithium ion battery cathode, *J. Phys. Chem. C.* 116 (2012) 4875–4882. <https://doi.org/10.1021/jp208428w>.
- [72] J. Chen, J. Liu, Y. Qi, T. Sun, X. Li, Unveiling the Roles of Binder in the Mechanical Integrity of Electrodes for Lithium-Ion Batteries, *J. Electrochem. Soc.* 160 (2013) A1502–A1509. <https://doi.org/10.1149/2.088309jes>.
- [73] Z. Lu, N. Liu, H.W. Lee, J. Zhao, W. Li, Y. Li, Y. Cui, Nonfilling carbon coating of porous silicon micrometer-sized particles for high-performance lithium battery anodes, *ACS Nano.* 9 (2015) 2540–2547. <https://doi.org/10.1021/nn505410q>.
- [74] N. Shpigel, M.D. Levi, S. Sigalov, O. Girshevitz, D. Aurbach, L. Daikhin, N. Jäckel, V. Presser, Non-Invasive in Situ Dynamic Monitoring of Elastic Properties of Composite Battery Electrodes by EQCM-D, *Angew. Chemie - Int. Ed.* 54 (2015) 12353–12356. <https://doi.org/10.1002/anie.201501787>.
- [75] R.L.M. Stuart, McCullough, Combining rules for predicting the thermoelastic properties of particulate filled polymers, polymers, polyblends, and foams, *Polym. Compos.* 2 (1981) 149–161. <https://doi.org/10.1002/pc.750020403>.
- [76] X. Zhang, W. Shyy, A. Marie Sastry, Numerical Simulation of Intercalation-Induced Stress in Li-Ion Battery Electrode Particles, *J. Electrochem. Soc.* 154 (2007) A910. <https://doi.org/10.1149/1.2759840>.
- [77] W.H. Woodford, Y.-M. Chiang, W.C. Carter, “Electrochemical Shock” of Intercalation Electrodes: A Fracture Mechanics Analysis, *J. Electrochem. Soc.* 157 (2010) A1052. <https://doi.org/10.1149/1.3464773>.

- [78] G. Bucci, T. Swamy, S. Bishop, B.W. Sheldon, Y.-M. Chiang, W.C. Carter, The Effect of Stress on Battery-Electrode Capacity, *J. Electrochem. Soc.* 164 (2017) A645–A654. <https://doi.org/10.1149/2.0371704jes>.
- [79] Y. Zhu, C. Wang, Strain accommodation and potential hysteresis of LiFePO₄ cathodes during lithium ion insertion/extraction, *J. Power Sources.* 196 (2011) 1442–1448. <https://doi.org/10.1016/j.jpowsour.2010.08.008>.
- [80] J. Gaubicher, F. Boucher, P. Moreau, M. Cuisinier, P. Soudan, E. Elkaim, D. Guyomard, Abnormal operando structural behavior of sodium battery material: Influence of dynamic on phase diagram of Na_xFePO₄, *Electrochem. Commun.* 38 (2014) 104–106. <https://doi.org/10.1016/j.elecom.2013.11.017>.
- [81] S.K. Soni, B.W. Sheldon, X. Xiao, A.F. Bower, M.W. Verbrugge, Diffusion Mediated Lithiation Stresses in Si Thin Film Electrodes, *J. Electrochem. Soc.* 159 (2012) A1520–A1527. <https://doi.org/10.1149/2.009209jes>.
- [82] V.A. Sethuraman, V. Srinivasan, A.F. Bower, P.R. Guduru, In Situ Measurements of Stress-Potential Coupling in Lithiated Silicon, 2010.